



# SFERA-III

## Solar Facilities for the European Research Area

### Material durability tests.

Deliverable D8.2

---

Estimated delivery date: 31.03.2022

Actual delivery date: 10.01.2022

Lead beneficiary: ETHZ

Person responsible: Brendan Bulfin

Deliverable type:  R  DEM  DEC  OTHER  ETHICS  ORDP

Dissemination level:  PU  CO  EU-RES  EU-CON  EU-SEC

---



## AUTHORS

Author	Institution	E-mail
Manuel Romero	IMDEA	manuel.romero@imdea.org
José González-Aguilar	IMDEA	jose.gonzalez@imdea.org
Mario Sánchez	IMDEA	mario.sanchez@imdea.org
Brendan Bulfin	ETHZ	bulfinb@ethz.ch
Sebastian Sas Brunser	ETHZ	sasbrunser@ethz.ch
Aldo Steinfeld	ETHZ	aldo.steinfeld@ethz.ch

## DOCUMENT HISTORY

Version	Date	Change
1	22.11.2021	First draft template
2	15.12.2021	ETHZ first draft - IR Furnace
3	07.01.2022	IMDEA draft review and input section 1
4	19.01.2022	Revised and final draft

## VALIDATION

Reviewers		Validation date
WP leader	Brendan Bulfin	19.01.2022
Project coordinator	Ricardo Sánchez	19.01.2022

## DISTRIBUTION LIST

Date	Recipients
22.11.2021	Task 8.1 contact list

## Disclaimer

The content of this publication reflects only the author's view and not necessary those of the European Commission. Furthermore, the Commission is not responsible for any use that may be made of the information this publication contains.

# Executive Summary

The use of concentrating solar energy for the production of solar fuels and chemicals implies making use of irradiances onto the solar reactor aperture well beyond the current state of the art in solar thermal power plants and requires making use advanced concepts of receivers, like particle receivers, able to withstand very high temperatures and solar flux. Particles solar reactors can be distinguished, according to the classification proposed, in entrained, fluidized and stacked reactors where materials are subject to extreme operational conditions involving attrition, cyclability, mechanical shocks, sintering and need of compatibility between chemically active compounds and inert insulation.

IMDEA Energy provides in Section 1 of this document information about a set of techniques and the procedures implemented for testing and analysing results obtained for advanced materials with improved mechanical properties in order to enhance structural resistance of solar fuel reactors. The techniques involve supervision of chemical reactivity, hardness and morphology changes after cycling tests. For the thermal treatment of materials and the realization of redox cycles, electrical furnaces are proposed to mimic the conditions to be observed in real on-sun tests.

The illustration of system and testing procedure, as well as cycle stability tests for an IR furnace is given in Section 2 by ETHZ exemplified with its own equipment.



## Table of Contents

---

<b>Executive Summary</b> .....	<b>3</b>
<b>Table of Contents</b> .....	<b>4</b>
<b>1. Testing advanced materials with improved mechanical properties.</b> .....	<b>5</b>
1.1. <i>Experimental procedures</i> .....	7
1.1.1. Analysis of reactivity .....	7
1.1.2. Structural analysis.....	9
1.1.3. Morphological analysis.....	10
1.1.4. Mechanical strength.....	13
1.1.5. Gas analysers.....	14
1.1.6. Furnaces .....	18
1.2. <i>Results</i> .....	21
1.2.1. Ceria pellets characterisation.....	21
1.2.2. Aging of pellets during thermochemical cycling.....	25
1.3. <i>Summary of procedures</i> .....	30
<b>2. IR furnace cycle stability tests at ETHZ</b> .....	<b>31</b>
2.1. <i>Experimental Procedures</i> .....	31
2.2. <i>Results</i> .....	34
2.3. <i>Summary of procedures</i> .....	36
<b>3. References</b> .....	<b>37</b>

# 1. Testing advanced materials with improved mechanical properties.

In recent years, significant progress has been accomplished in the development of CSP (Concentrating Solar Power) systems making use of heliostat fields, with central receivers on top of a tower, capable of achieving irradiances well above 2000kW/m<sup>2</sup>. Such high solar radiation fluxes allow the conversion of solar energy to thermal reservoirs well beyond 1000°C, which are needed for the more efficient two-step thermochemical cycles using metal oxide redox reactions, either for use in thermochemical energy storage (Carrillo et al., 2019) or for the production of solar fuels (Romero and Steinfeld, 2012).

The use of concentrating solar energy for the production of solar fuels and chemicals implies making use of irradiances onto the solar reactor aperture well beyond the current state of the art in solar thermal power plants and requires making use advanced concepts of receivers, like particle receivers, able to withstand very high temperatures and solar flux (Alonso and Romero, 2015). Particles may be arranged with different configurations depending on their required residence time inside the reactor and the existence of a carrier fluid and its contact mode with the particles. These parameters affect directly to the heat and mass transfer occurring inside the reaction zone. Thus, particles solar reactors can be distinguished, according to the classification proposed, in entrained, fluidized and stacked reactors where materials are subject to extreme operational conditions involving attrition, cyclability, mechanical shocks, sintering and need of compatibility between chemically active compounds and inert insulation. IMDEA Energy provides illustration herewith on techniques for testing advanced materials with improved mechanical properties in order to enhance structural resistance of solar fuel reactors.

Materials require suitable shaping for the operation at the different types of solar reactors like entrained, fluidized or stacked as granules, pellets, foams or monoliths, therefore a technique is required for the synthesis and preparation of pellets, granules or volumetric absorbers. In this report, target raw materials are Ceria and CMC-Carboxy-Methyl-Cellulose extruded 2.5 mm for formation of porosity after calcination.

Supervision of chemical reactivity, hardness and morphology changes after cycling tests and in general the necessary techniques for physicochemical supervision are presented, being classified as follows

- Reactivity
  - Thermogravimetry TGA
  - Thermal Programmable reduction (TPR)
- Structural analysis
  - XRD
- Morphological analysis.
  - SEM
  - Optical microscopy
  - Image analysis
- Mechanical strength (Dynamometer)
- Gas analysers
- Electrical furnaces
  - Furnace for material treatment
  - Vertical furnace for redox tests
  - IR horizontal furnace for redox tests

The illustration of system and testing procedure for the IR furnace is given in Section 2 by ETHZ exemplified with its own equipment. The rest of specific equipment and techniques described in Section 1, correspond to the ones commonly used by IMDEA Energy.

The experimental procedure is illustrated with Ceria, since it is currently considered as the reference metal oxide to produce hydrogen via solar thermochemical cycles (Muhich et al., 2018), and it has also been extensively investigated to produce syngas (Zoller et al., 2019). This material is proven to be chemically stable for thousands of cycles (Rhodes et al., 2015). Although new mixed metal oxides, such as perovskites, provide better fuel production rates (Bork et al., 2020), these novel materials are not as stable as ceria under cyclability.

Moving to final on-sun application requires additional aging test to analyse some features considering the reactive material conveniently shaped (as foams, pellets...) for the solar reactor, and demonstrate compatibility between reactor materials at expected operating conditions. In particular, ceramics such as alumina, silica, or mullite are

extensively employed to isolate the receivers (Haeussler et al., 2020; Zoller et al., 2019). In this regard, reports on the alteration of Ceria crystal structure by forming mixed metal oxides can be found in the literature (Costa Oliveira et al., 2018).

Some authors propose isothermal redox cycling is feasible and avoids the solid-solid heat recuperation and material stability challenges associated with temperature swing (about 400°C); by using iron aluminate-based spinel solid solutions that preferentially exhibit large changes in oxygen content within the range of oxygen partial pressures expected in large-scale systems (Warren, Tran and Weimer, 2002), however still the operation requires high solar flux and temperatures above 1400°C.

## **1.1. Experimental procedures**

### **1.1.1. Analysis of reactivity**

To analyse the performance that the materials used have in conditions similar to those that will later be tested experimentally, as well as to characterize the processes for shaping of the materials, thermogravimetric tests are carried out. In addition, to check the effect that the different tests have on the reactive materials used, temperature-programmed reduction techniques are proposed.

#### **Thermogravimetric Analysis**

This technique, TGA, is based on the measurement of mass variation, as well as the heat emitted or absorbed by a solid sample when subjected to different temperatures controlling the atmosphere in which it is located.

In case of knowing all the reactions that take place when applying each of the conditions, from this difference in mass it may be possible to obtain parameters such as the progress of the evolution of each reaction.

The equipment used to perform this analysis is a thermobalance model SDT Q600 from TA Instruments. This equipment has the possibility of carrying out the tests by alternating inert gas (argon) and air flows. The temperature at which this system can work in a timely manner is 1300°C, being able to maintain isotherms of up to 1100°C.

### **Temperature-programmed reduction**

Temperature Programmed Reduction (TPR) consists of, by fixing the flow rate and concentration of a gaseous reducing agent, observing how this last property varies after passing through the solid sample object of the study. Through these data, the reduction status of the analysed sample can be deduced.

To carry out these tests, the AutoChem II 2920 equipment from Micrometrics is used, which, in addition to TPR, can perform desorption and oxidation studies at a programmed temperature by using different gaseous streams. The system shown in Figure 1 has a steam generator, not used in the studies carried out and a furnace capable of reaching 1100 °C. Inside this furnace it is placed the solid sample to be analysed, fixed by a bed of rock wool in a U-shaped tube. After passing through the furnace, the gases reach a cold trap for the removal of condensable products that can damage the sensors and finally reach a thermal conductivity detector that measures the composition of binary mixtures continuously.



Figure 1. **Chemisorption equipment AutoChem II 2920 from Micrometrics.**

This equipment is used for the characterization of the aging suffered by the reactive materials used in the tests. The way to measure the condition in which the aged material is, consists of comparing the degree of reduction that the material is able to achieve, once used, with the reduction obtained by using different reference materials.

These references are samples of the same nature with which no tests have been carried out in the reaction testing systems.

### 1.1.2. Structural analysis

In order to know the composition and crystal structure of the materials used, the X-ray diffraction technique is used.

#### X-ray Difraccion

This technique is based on Bragg's law. Figure 2 shows a simplified scheme of this law, in which the different atomic layers that form the crystal structure are represented on the plane. The distance between these layers is characteristic of the crystal structure and the material.

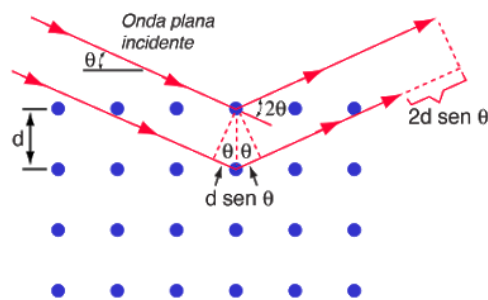


Figure 2. **Scheme of Bragg's Law**

When light beam, X-rays in this case, hits the surface of the solid at a certain angle  $\theta$ , part of it is diffracted by the first layer as shown in the diagram above. However, this radiation is able to penetrate the structure and produce diffractions in the inner layers of the solid. This diffraction will only be in phase with that produced in the first layer; that is, it will be constructive, when the incident wavelength, or any of its integer multiples, is equal to twice the distance between atomic layers by the sine of the angle of incidence, as described in equation (1).

Equation 1

$$n\lambda = 2d \cdot \sin \theta$$

Thus, knowing the characteristics of the incident beam and making a sweep for different angles of incidence ( $\theta$ ), the distance between atomic layers that are characteristic of each material and crystal structure can be calculated.

Subsequently, the signal obtained is compared with data from bibliographic references of the materials that could be present in the analysed sample. In this way, the presence of each of the expected phases is determined with the help of references by analysing the position and relative intensity of each of the detected peaks.

To carry out this analysis, the Empyrean diffractometer model of PANalytical has been used, with a PIXcel<sup>3D</sup> receiver. The monochromatic radiation used is that corresponding to the K $\alpha$  line of copper (1.548 Å). By coupling this diffractometer to a computer equipment in charge of processing the signal of the equipment, the diffractograms are obtained.

### 1.1.3. Morphological analysis

The study of the size and shape of the materials tested is performed using Scanning Electron Microscopy (SEM), optical microscopy and image analysis at the macroscopic level.

#### Scanning Electron Microscopy

This technique is used for the analysis of the shape and size of the crystals formed during the sintering processes of the materials used in the different reactors developed by generating a three-dimensional image of the analysed sample.

To achieve this, the microscope emits an electron beam that is collimated and focused by a set of electromagnetic lenses on a point of the sample to be treated. Depending on the material studied, mainly on the molecular weight of the substance to be treated, the detector quantifies the secondary or backscattered electrons that are subsequently translated into a monochromatic scale. This process is repeated over the total surface to be observed, generating the image that is extracted from the device.

The equipment used to perform this characterization is a HITACHI TM-1000 tabletop

microscope, capable of providing up to 10000x magnification. The samples were supported on carbon adhesives.

### **Optical Microscopy**

In order to characterize and monitor the changes that take place during experiments on the morphology of the materials used, optical microscopy is used. This technique allows, through a series of optical lenses, to observe in detail the surface of the samples, generating a stereoscopic image that can be captured through a camera.

To perform this analysis, a digital stereographic microscope model SZ61 – TR by Olympus has been used. This device generates images magnified up to 90 times and has an attached digital camera that allows collecting high-resolution images in the entire range of magnifications in which the system can operate.

### **Image processing**

In order to measure the homogeneity of the pellets used in the experimental process, an algorithm is designed to identify them. Subsequently, both its radius and length are measured. To do this, photographs must be taken of a group of particles that is treated by an algorithm implemented in MatLab. The procedure followed for taking these measurements is detailed below.

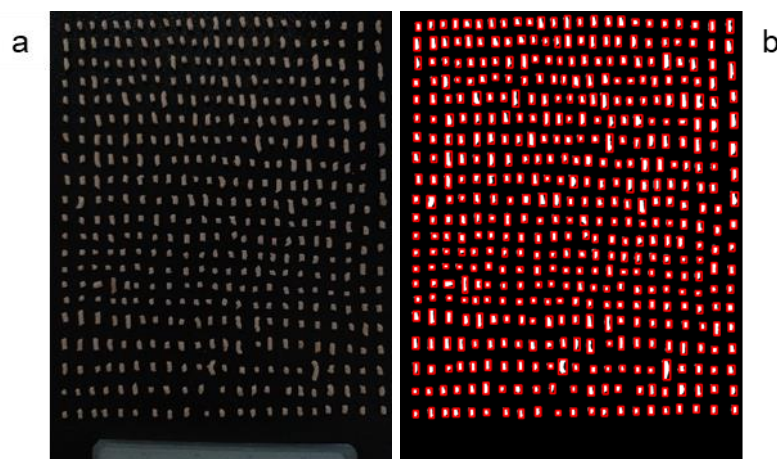


Figure 3. **Binary image of particles (a) before noise removal (b) after noise removal**

First, a picture of the particles to be measured is taken along with a reference frame, as shown in Figure 3(a), in which all the particles are so that the radius coincides with the horizontal axis of the image. For the system to work properly, it is necessary that there is a great contrast between the background and the rest of the image to be treated.

This image is cropped manually, generating one in which only the reference frame is found and another in which all the particles to be measured appear. Subsequently, the first one is taken and the number of pixels between each mark of the measurement system used is calculated, generating from the average of all of them the relationship between pixels and millimetres.

Next, the second part of the image is taken, in which the pellets to be measured are found, and translated into a binary image, to facilitate calculations and reducing the size of the images generated. The BoundingBox property of MatLab is then applied to recognize all edges, resulting in the detection of the particles as shown in Figure 3(b).

Each of the particles detected in the previous step is stored in a separate file. Subsequently, the image is digitally rotated so that both dimensions are as straight as possible with the horizontal and vertical axes. The effect of this adjustment can be seen in the difference between Figure 4. It shows one of the particles as it was detected (Figure 4(a)) and after making the rotation adjustment on it (Figure 4(b)).

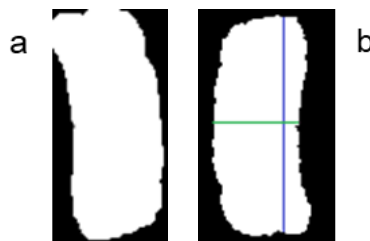


Figure 4. **Detail of results of a pellet (a) Before orientation correction (b) After orientation correction**

Finally, a horizontal and a vertical sweeping is carried out in which the number of white pixels in each of the generated and corrected images is counted and this value is translated from pixels to millimetres by using the relationship calculated above. The value adopted as correct for the diameter and height of each of the particles respectively is the highest of those calculated to avoid interference generated by

particles with non-cylindrical shapes.

Particle size distribution and pellet volumes once determined by image processing using the in-house Matlab-based code of pellet photographs, together with the mass measurement of the same particles lead to assess the mean density,  $\rho_{\text{pellet}}$ . Using ceria bulk density,  $\rho_{\text{CeO}_2}$ , as reference ( $7220 \text{ g cm}^{-3}$ ), particle porosity can be calculated as

Equation 2

$$\varepsilon_{\text{pellet}} = 1 - \frac{\rho_{\text{pellet}}}{\rho_{\text{CeO}_2}}$$

#### 1.1.4. Mechanical strength

To measure the mechanical strength of the solids studied, a Dynamometer model Chatillon DFS II-100 of the Ametek brand is used as shown in Figure 5. This device can measure up to 500 N of compressive force to be performed on the plate where the samples are located.



Figure 5. **Dynamometer Ametek Chatillon DFS II-100**

The pellets treated with this technique are placed on their lateral side to measure the force that needs to be applied before it fractures. The equipment used works manually

and the analysis is destructive, so this technique is only applied to ten randomly chosen pellets within each study group.

### **1.1.5. Gas analysers**

There is a conditioning system and two types of analysers to know the nature of the gases at the exit of the reaction system: continuous and chromatographic analysers. The latter can be considered semi-continuous because they are used taking measurements uninterruptedly throughout the experiment, but obtaining results with a frequency of several minutes depending on the analysis method used.

#### **Conditioning system**

To ensure that the gases reach the analysers completely dry and at the optimum working temperature, the analysis bench includes a CSS-V1 conditioner from M&C. Its role is to remove the possible moisture contained in the gas and expel it through a peristaltic pump to an adjacent tank. For this, it has a gas cooler with a maximum power of 40 W. In addition, it has a filter capable of retaining particles up to 0.3  $\mu\text{m}$ .

This equipment supports a maximum flow rate of 4  $\text{L}\cdot\text{min}^{-1}$ , well below the setpoint flow of continuous analysers, which guarantees its correct operation.

#### **Continuous analysers**

The continuous analysis equipment used has been Ultramat 23 and Calomat 6, both developed by Siemens. The former measures the concentration of oxygen, carbon dioxide, carbon monoxide and methane, while the latter only analyses the amount of hydrogen present in the output gases. Both systems have rapid measuring rates that are translated into a signal of 4-20 mA. This signal is analysed and transformed by the control program developed in LabView into concentration measurements for saving and subsequent treatment. Due to the long duration of the experiments and in order not to saturate the memory of the control computer, the frequency of data collection is set at one second.

The Ultramat 23 analyser features detection systems for active infrared compounds, such as methane, carbon monoxide and carbon dioxide, measured using multilayer non-dispersive infrared radiation (NDIR) sensors. In the case of oxygen, the system

uses a paramagnetic detector. This analyser has a flow meter on its front, being calibrated for a gas flow of  $1 \text{ L}\cdot\text{min}^{-1}$ . To obtain it, it has an internal pump, although in the uses given to this equipment in the experimental development a valve system has been used to direct this flow to the analysis bank, the rest being safely vented. The equipment used also has a self-calibration function that adjusts the oxygen concentration, each time the equipment is turned on or at the request of the user, using atmospheric air as a reference.

The Calomat 6 analyser measures the hydrogen concentration through the specific thermal conductivity of the mixture. It has an adjustable measurement range in four levels to fix the accuracy of the electrical signal it emits to the data acquisition system as shown in Table 1. The main problem presented by this device is the inability of it to discern the concentration of hydrogen from a stream containing nitrogen, since the detector attributes approximately 0.13% v of hydrogen to every 1.00% v of nitrogen present in the system. This is one of the reasons that motivate the use of argon as a carrier gas in particle receivers.

Table 1. **Range of concentrations of analyser Calomat 6.**

Level	Range (% <sub>v</sub> H <sub>2</sub> )
<b>1</b>	0-1
<b>2</b>	0-5
<b>3</b>	0-25
<b>4</b>	0-100

### **Chromatographic analysis**

The chromatographic analysis of the gas stream obtained from the reaction system is performed using the Agilent 490 gas microchromatograph. The system used allows the installation of up to four independent acquisition channels. Each of them consists of an electronic gas microcontroller, an injector, a column and an independent detector. In addition, within the analysis method each of the channels can define its own conditions of injection volume, injector and column temperatures, pressure and carrier gas used.

## **Micro Electronic Gas Control (Micro EGC)**

The Micro Electronic Gas Control adjusts the column pressure. This can be constant or programmed to vary throughout the trial. This pressure sets the flow rate that passes through the column, being able to take values from 50 to 350 kPa. This results in a carrier gas flow rate of between 0.2 and 4.0 mL min<sup>-1</sup>.

## **Injector**

The injector of this system is a coil with a capacity of 10 µL that is filled with the sample gas at a pressure between 0 and 100 kPa. In this section you can set the injection time, usually set at 40 ms. This time determines the amount of sample to be analysed, which for the aforementioned time means an injected volume of around 200 nL.

## **Columns**

The three channels used out of the four available on the computer have different configurations. Channels 1 and 2 have 10 m long Molsieve 5Å columns. In the case of the first channel, it uses argon as the carrier gas, while the second uses helium. This column is used for the analysis of permanent gases such as oxygen, nitrogen, hydrogen, carbon monoxide, etc.

The third channel has a Pora Plot Q column installed that uses helium as a carrier gas. This column is used to analyse light hydrocarbons (up to C6) and other volatiles such as carbon dioxide, or hydrogen sulphide in addition to light solvents.

## **Detector**

The system has a thermal conductivity detector (TCD) installed. This detector works by comparing this parameter in two different cells. Through the reference only the carrier gas passes while through the other one it is passing the stream coming from the column. By containing one of the separate elements in the column, the conductivity of the current changes, causing the variation of this signal as a function of time due to the difference in temperature at which the gases leave both cells.

## **Equipment Configuration**

The first channel is configured with the column at a temperature of 90°C and a

pressure of 150 kPa. In the second, the temperature is set at 120°C and the pressure at 150 kPa and in the third the pressure is 100 kPa and the temperature of the column is 50°C.

In all cases the injection time is 40 ms and a sampling time of 20 s is set to ensure that the pump is able to purge all the gas that is in the aliquot that goes from the path that feeds the continuous analysers to this analyser.

With this configuration, sufficiently defined peaks are achieved with a maximum data collection time of 75 s for the case of the second channel as can be seen in the data from one of the calibrations carried out in Figure 6.

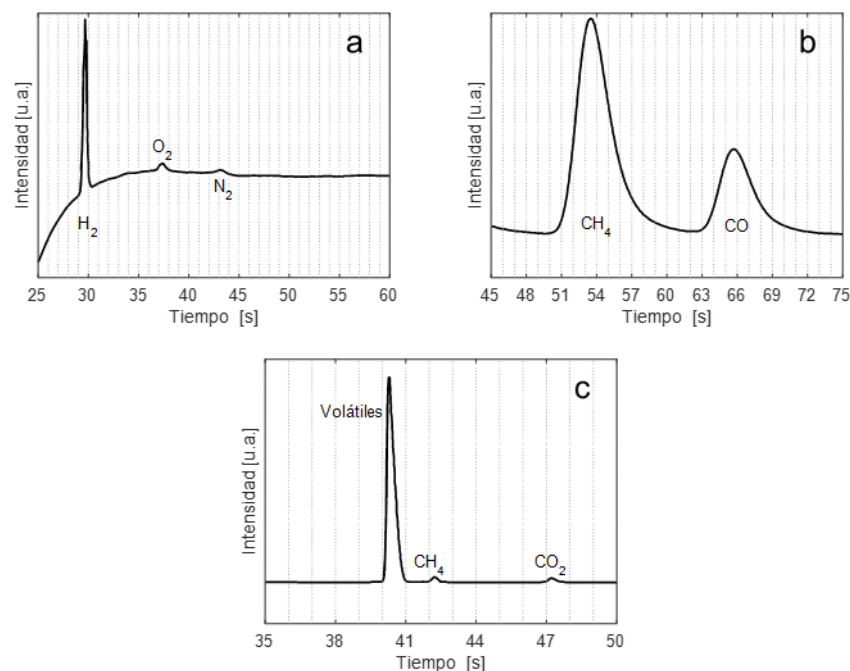


Figure 6. **Calibration chromatogram for (a) Channel 1 (b) Channel 2 and (c) Channel 3**

The first peak appearing in the third channel (Figure 6(c)) corresponds to the sum of all the non-condensable gases present in the sample, including argon used as a transport gas. Despite their proximity to the methane peak, the system has sufficient resolution to distinguish them and accurately measure the concentration of hydrocarbons in all the points studied.

## 1.1.6. Furnaces

Under this heading, the different furnaces used are divided according to their final use, distinguishing between the furnace used for the thermal treatment of materials and the vertical tubular furnace used to heat the reaction system. In addition, another infrared gold image horizontal furnace is presented by ETHZ in Section 2, below.

### **Material treatment furnace**

To carry out the sintering processes, the Nabertherm LHT 04/16 high temperature furnace has been used. This furnace has a 4-liter chamber and can reach a maximum temperature of 1600°C.

The heating power of the system is 5.2 kW, which allows to reach the maximum working temperature from room temperature (25°C) in 25 min.

### **Vertical tubular furnace**

To heat the hot reaction system and conduct redox cycles with a sufficient amount of shaped material, a customized equipment, capable of providing the extreme temperatures that are required to carry out the processes, has been developed by IMDEA Energy.

Applying all the operational specifications, Hobersal Furns designed and built the ST17-6V3Z closed-tube furnace.

Figure 7 shows the equipment before the installation of the reactor, as well as some details of its construction.



Figure 7. **Vertical tube furnace ST-6V3Z**

This furnace has a maximum power of 15 kW distributed equally in the three marked areas. Each of them has six electrical resistances and a thermocouple for temperature control, being able to control each of the zones independently. The maximum working temperature of this equipment in a timely manner is 1700°C, being reduced to 1600°C in case of working at a sustained temperature for long periods of time.

Each of the three zones has a length of 20 cm, so the total length of the heated area is 60 cm. This whole area is isolated from the outside by alumina ceramic bricks and has a ventilation system to cool the steel box that surrounds the hot zone. It is supported on a steel structure so that the bottom of the furnace is at 1 m height, thus allowing to comfortably work both at the bottom and top of it.

In the Figure 8, it can be seen the scheme used for the vertical tube furnace by IMDEA Energy to obtain a flexible testing of Ceria and perovskites powder, pellets, granules and monoliths, both at fixed and fluidized bed conditions.

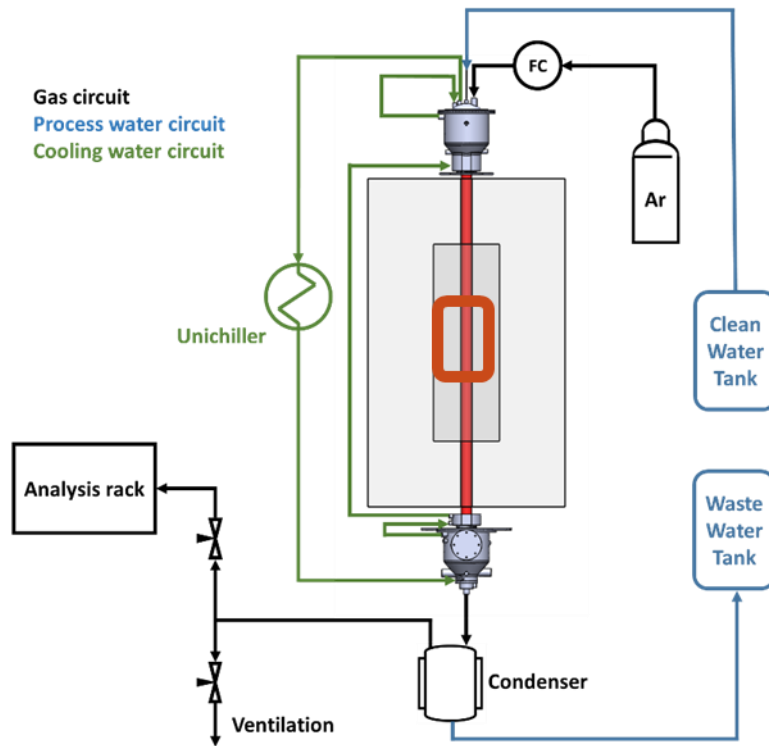


Figure 8: **Scheme of vertical furnace system.**

The total tube length is 1.2 m and the heated area of the vertical furnace is 60 cm and as already mentioned divided in three independent zones. The 10 cm packed bed composed of 80 g of ceria pellets was placed in the centre of the heated section of the tube supported by a packed bed made of coarse mullite (Al<sub>6</sub>Si<sub>2</sub>O<sub>13</sub>) particles.

Typically, tests were performed by fixing two of the parameters and changing values for the third one (temperature, steam concentration and total mass flowrate). The table below shows an example of tests performed for 80 g of CeO<sub>2</sub> particles.

Table 2. **List of temperatures, steam concentrations and mass flowrates tested.**

Test	Temperature (°C)	Steam Concentration (% w)	Total mass flow
Temperature	1200 - 1300	56	730
Concentration	1500	10 - 25 - 50 - 75	730
Flow	1500	75	500 - 730 - 1000 - 1250 - 1500 - 1940

In the example illustrating the testing, Ceria pellets were produced in-house. A homogeneous mixture composed of water,  $\text{CeO}_2$  powder and carboxymethylcellulose (CMC) was prepared to procure 3 mm thick extrudates that then are cut into 3.5 mm long pellets. The pellets were firstly dried at ambient temperature and followed by a thermal treatment designed to complete the drying process, remove the CMC and sinter the ceria. To finalise CMC calcination and sintering, the temperature was raised and then maintained up to 4 h at 1773 K.

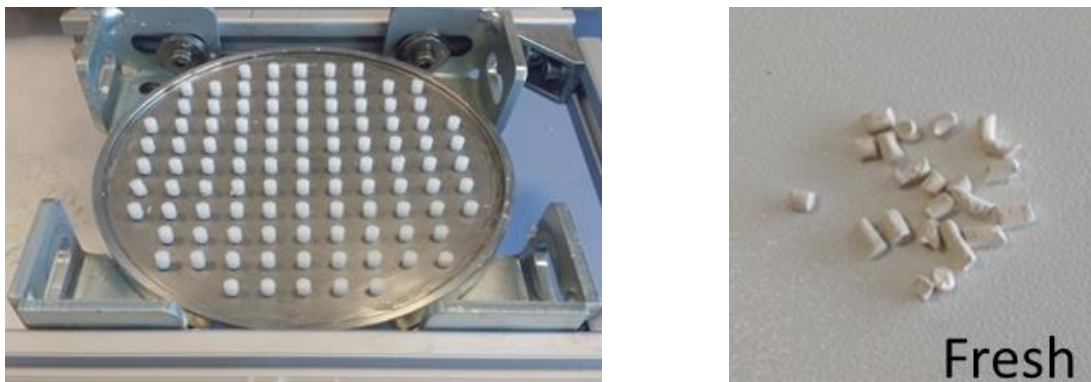


Figure 9. **(Left) Shaping of Ceria pellets (Right) Ceria wet pellets fresh prior to thermal treatment**

## 1.2. Results

### 1.2.1. Ceria pellets characterisation

Overnight-dried pellets are greyish cylindrical granules (Figure 10, left) with a narrow diameter size distribution defined by the manufacture by extrusion. In this regard, 85% of pellets have diameters between 2.00 and 2.50 mm. Pellet size distribution in length is larger because they were cut manually, with 65% of granules in the range between 2.75 to 3.75 mm. CMC represents 33% of the pellet mass at this stage, but SEM micrograph in Figure 11(left) of the overnight-dried pellets show a porous CMC substrate decorated with  $\text{CeO}_2$  particles of different sizes. This is due to the lower density of CMC compared to ceria.



Figure 10. **Photos of (left) overnight-dried and (right) sintered fresh ceria pellets**

The calcined pellets present substantial physical changes, as illustrated in Figure 11, right. They have a pink colour and smaller size than just dried pellets due to CMC removal and ceria sintering. Diameter and length size distributions are shifted with respect to those of dried pellets by approximately 0.5 mm. SEM images (Figure 11, right) show the porous structure composed of sintered pure  $\text{CeO}_2$  grains with a typical size smaller than 10  $\mu\text{m}$ . The measured mass loss after calcination is 37%. Experimental mass and volume measurements lead to an estimated sintered pellet porosity of 0.7 (using Eq. (2)). In case of pre-sintered particles, this parameter cannot be properly calculated because the uncertainty on industrial grade CMC density employed as binder.

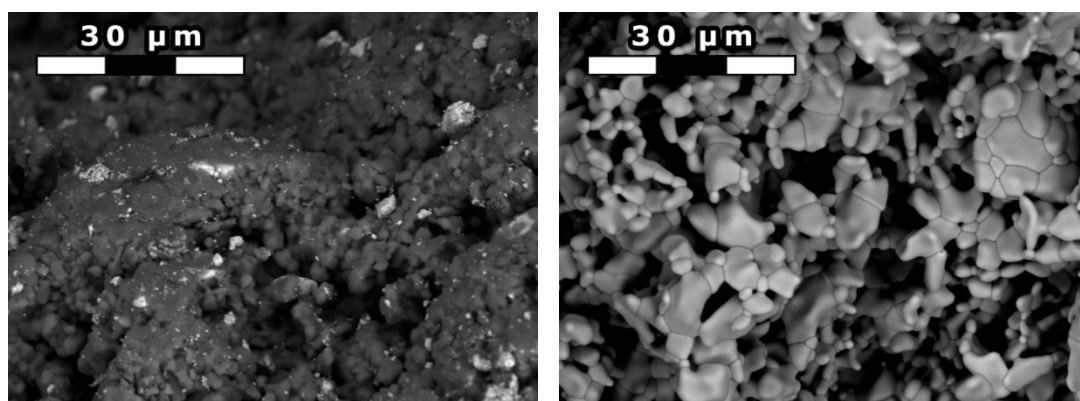


Figure 11. **SEM images of: (Left) Pre-sintered pellets (Right) Sintered fresh pellets. Horizontal bar length corresponds to 30 micrometres.**

Crushing strength measurements under compression concluded that just dried pellets were able to withstand forces as high as 300 N (upper limit of the Chatillon gauge) due to the presence of CMC binder. Pellets calcined at 1173 K, on the contrary, were very fragile due to binder removal. In turn, sintered pellets broke under an average compression force of  $70 \pm 10$  N, which indicates increased mechanical strength obtained by sintering of ceria particles.

The following table summarizes the findings obtained in the pellets with the selected techniques for the Ceria pellets before and after thermal treatment in the furnace.

**Table 3. Physical properties measured and estimated for pellets fresh and after sintering.**

Type	Diameter (mm)	Length (mm)	Mass (mg)	Crushing strength (N)	Density pellets ( $\text{kg} \cdot \text{m}^{-3}$ )	Porosity pellets	Porosity bed
Before sintering	$2.2 \pm 0.2$	$3.6 \pm 0.8$	$25.0 \pm 0.1$	N/A >300	$1.7 \pm 0.7$	$0.7 \pm 0.3$	$0.36 \pm 0.05$
After sintering	$1.8 \pm 0.1$	$3.0 \pm 0.8$	$15.7 \pm 0.1$	$70 \pm 10$	$2.0 \pm 0.8$	$0.7 \pm 0.3$	$0.27 \pm 0.09$

Finally, as a reference to measure the aging of the material in the following tests, 4 reduction tests are carried out at programmed temperature using particles and 3 using the ceria powder used to make the pellets. The same solid, whether in pellet or powder form, was used in all reduction tests. Between each of them, a calcination stage was carried out to re-oxidize the material and restore it to its original oxidation state. For this, the same temperature profile was used as during the heat treatment of the particles. Thus, at the beginning of each of the reduction tests it is considered that the material was completely oxidized.

In the case of pellets (Figure 12), there is a clear degradation between the results obtained in the first cycle and the subsequent ones. During the first cycle, the material begins to reduce at a temperature of  $400^\circ\text{C}$ . From this moment on, the material is reduced at a constant rate until the temperature reaches  $700^\circ\text{C}$ . Once this temperature is reached, the speed of vacancies production increases, being also

constant until the system reaches the isotherm of 900°C, which causes a new decrease in hydrogen consumption. However, this isotherm is not enough for the system to reach equilibrium, so the value of  $\delta$  continues to rise until the end of the experiment. The first phase of the reduction is attributed to the important surface area presented by the particles, while the second faster stage is due to the importance that the phenomenon of solid diffusion gains at high temperatures (Giordano et al., 2000). On the other hand, the degree of reduction obtained by the pellets once this first cycle is finished is 0.22. This value is within the reference values consulted, which place it between 0.20 and 0.27 (Yao and Yao, 1984).

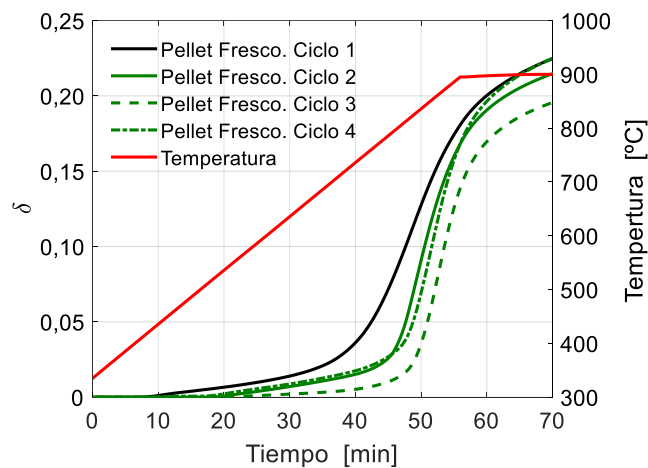


Figure 12. **Aging analysis via TPR of fresh ceria particles, cycles 1 to 4.**

From the second cycle a shift in temperatures to the right is observed due to the decrease in the porosity of the particles. By repeating cycles of reduction and oxidation that include high temperatures, the grains that make up the material grow and restructure, causing a decrease in the available surface. Therefore, to reach levels of speed of production of vacancies similar to those observed during the first cycle, it is necessary to increase the temperature. The temperature at which the reduction of the material begins increases to 550°C, which is identified with the beginning of the reduction process through the solid itself, ceasing to be only controlled by the surface of the material analysed (Wang and Makkee, 2018).

However, there is no clear trend in the last three cycles carried out. Although cycles 2

and 3 show a significant decrease in the generation of vacancies compared to the first, the third recovers levels of reducibility similar to those observed in the test carried out with fresh material. Even so, all cycles are within the range provided in the literature (Yao and Yao, 1984), obtaining  $\delta$  values of 0.21, 0.20 and 0.22 for cycles 2, 3 and 4 respectively. Therefore, as a reference for aged material, the curves obtained for cycles 3 and 4 are used, as they present more discordant values in terms of vacancies generated for these last three cycles.

### 1.2.2. Aging of pellets during thermochemical cycling

Once the hydrogen production experiments have been carried out, the reactive material used is recovered. The pellets analysed show two different colorations (Figure 13) that are characterized separately. On the one hand, pink particles are studied, which have a paler tone than that of fresh particles after heat treatment but before being used in the experimental device. The other group is made up of blue particles. This coloration is due to the fact that these have reached higher levels of reduction and, therefore, the amount of  $\text{Ce}^{3+}$  ions is greater than in the rest of the particles, although in both it is expected that a majority concentration of  $\text{Ce}^{4+}$  (Matsukawa et al., 2018).



Figure 13. **Photograph of part of the particles recovered after hydrogen production experiments**

Figure 14 shows the micrographs taken with the optical microscope for a pellet from each of the studied groups. In them it is observed how the pink particles (Figure 14 (a)), show a rough but uniform surface at this level of magnification. However, in the blue particles (Figure 14(b)) large holes and cracks in the surface are observed. Inside them it seems that the material is molten in what looks like amorphous structures. However, this cannot be verified in the analysis performed with scanning electron microscopy (Figure 15(b)), where the structure is uniform and similar to that of the particles before use.

The presence of these apparently molten zones is consistent with the coloration of the blue particles. Cerium oxide has a melting point of  $2100^{\circ}\text{C}$ . At this temperature, the degree of oxidation achieved by the ceria in the absence of oxygen is close to that fixed by stoichiometry. One of the factors that can favour this punctual and local increase in temperature is the process of adsorption of steam before hydrolysis, as this is an exothermic process (Molinari et al., 2012).



Figure 14. **Optical micrographs of ceria particles used for hydrogen production: (a) pink particles (b) blue particles**

The particles are then analysed using SEM (Figure 15). Comparing these micrographs with those taken from the material before use, a significant increase in grain size and a decrease in porosity are observed in both cases. This phenomenon is due to the high

working temperatures induced for long periods of time, which favour the sintering of the material. In this way, it is clear that there is no substantial difference in grain size, if the connections between them have been greatly increased, resulting in a much more compact structure.

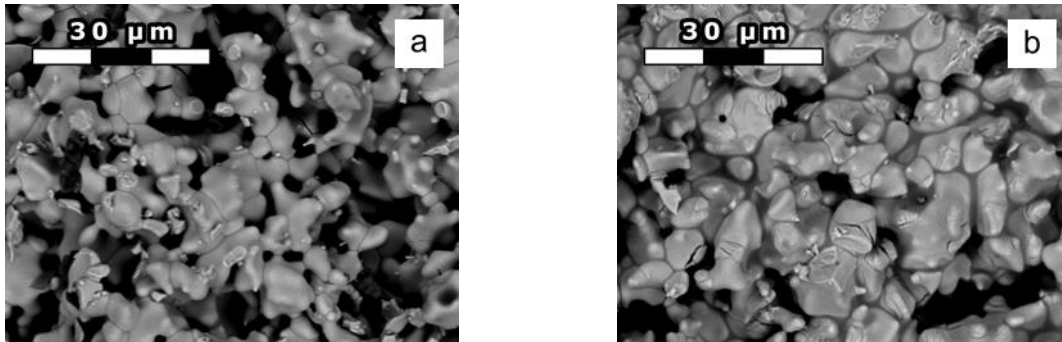


Figure 15. **SEM microscopy images of ceria particles used in hydrogen production tests: (a) Pink particles (b) Blue particle**

Directly comparing the images of the two types of particles recovered, a greater degree of compaction is observed in the blue particles. This is due to the high temperatures that, locally, have led the material to melt and shrink by more than the rest.

The physical properties of the recovered particles are then measured. Compared to those used in the analysis of the heat treatment process the particles selected in this case have a longer average length, maintaining a similar diameter. This results in an increase in mass per particle measured. Therefore, to compare the evolution of this characteristic, the focus must be on the bulk density of the pellet. In both cases there is a considerable increase in this property (30% for pink particles and 60% for blue particles). This fact subsequently translates into increases in the porosity of the particles for both cases. This phenomenon is in line with what is observed in Figure 15, where it is observed how the interactions between the grains of the particle increase for these two cases compared to the fresh particles, generating more compact particles.

**Table 4. Physical properties measured and estimated for the pellets (pale pink and blue) after redox cycles for H<sub>2</sub> production.**

Type ceria	Diameter (mm)	Length (mm)	Mass (mg)	Crushing strength [(N)	Density pellets (kg·m <sup>-3</sup> )	Porosity pellets	Porosity bed
Pale pink	1.8 ± 0.1	3.5 ± 0.5	23.0 ± 0.1	50 ± 20	2.6 ± 0.9	0.6 ± 0.2	0.3 ± 0.1
Blue	1.7 ± 0.1	3.4 ± 0.4	24.8 ± 0.1	80 ± 30	3.2 ± 0.8	0.5 ± 0.2	0.4 ± 0.2

However, the porosity of the bed observed does not seem to vary when compared to the particles treated before use. This is because the size of the particles, characterized by their diameter and length, undergoes negligible changes, so the degree of compaction of the bed remains stable. However, in the case of the particles used, the uncertainty in this measure is greater.

Finally, in terms of crushing strength, pink particles show a drop in measurements of 21% compared to fresh pellets. In the case of blue particles, more compact, the average of the measurements made is 14% higher than that of unused pellets. However, in both cases the deviation of these data is much higher than that observed for fresh particles.

On the dust generated during the tests of resistance to the crushing of these particles, the X-ray diffraction analysis, shown in Figure 16, is performed. As can be seen, the use of particles has no effect on crystalline structures, presenting the same profile as that observed for sintered particles for both blue and pink particles.

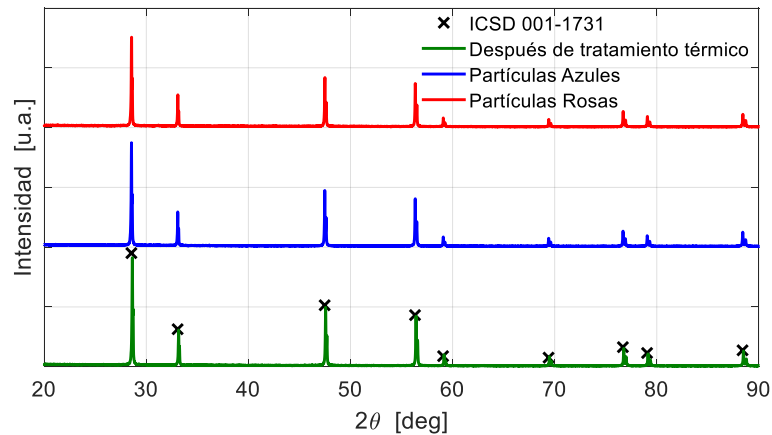


Figure 16. **X-ray diffraction of particles used for hydrogen production**

Figure 17 shows the TPR analysis performed on a mixture of pink and blue particles with the particles as obtained from the reactor (Prod. H<sub>2</sub> Fresh). The reduction process begins at a temperature of around 500°C, as in the case of fresh particles analysed from the second cycle. This implies that the surface reaction is practically deactivated. The phenomenon that is causing it, is the compaction of the particles that can be seen in Figure 15. However, this decrease in surface activity is partially offset by the increase in contact points between particles. That is why the early stages of reduction have speeds similar to those observed for the particles during their first treatment. However, as the temperature increases, the gases find greater resistance to access the inner part of the particles, causing the speed to decrease until reaching values of  $\delta$  similar to those observed for the particles analysed from the second cycle.

A second batch of particles was calcined using the heat treatment (Prod. H<sub>2</sub> Calcined). In this case, the deactivation of the reaction on the surface is in line with what is observed in the fresh particles used. However, as the temperature increases, the number of vacancies generated does not reach the reference material, due to a fall in the porosity of the pellets more important than that observed in the reference.

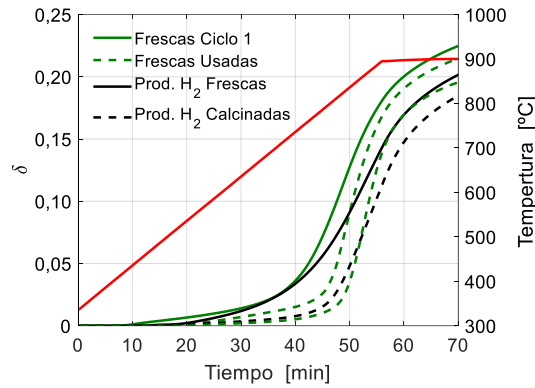


Figure 17. **TPR analysis after use for the production of hydrogen**

### 1.3. Summary of procedures

Structure and composition of ceria pellets were characterized by scanning electron microscopy (SEM) employing a Hitachi T-1000 microscope and X-Ray diffraction (XRD) using an Empirean diffractometer from PANalytical. The monochromatic radiation needed for this last device was Cu K $\alpha$  ( $\lambda = 1.54$  nm).

Particle size distribution and pellet volumes were determined by image processing using an in-house Matlab-based code of pellet photographs. This analysis together with the mass measurement of the same particles lead to assess the mean density,  $\rho_{\text{pellet}}$ . Using ceria bulk density,  $\rho_{\text{CeO}_2}$ , as reference ( $7220 \text{ g}\cdot\text{cm}^{-3}$ ), particle porosity was calculated.

Finally, mechanical strength under compression was tested using a dynamometer (Chatillon DFS II-100 Ametek). The cylindrical pellets were placed resting on their lateral side for this purpose.

The chemical behaviour of the pellets was studied by temperature programmed reduction (TPR) tests using an AutoChem II 2920 (Micrometrics). During these tests, the sample temperature increased from 300 to 1173 K at  $10 \text{ K}\cdot\text{min}^{-1}$  under  $50 \text{ cm}^3\cdot\text{min}^{-1}$  flow of 10%vol. H $_2$  in Ar. Afterwards, this temperature remained constant for 30 min. The reducibility of the material was evaluated by monitoring H $_2$  consumption as a function of temperature. Finally, redox cycles were conducted in a vertical furnace for 80 g CeO $_2$ , for the production of H $_2$  from steam and for the reduction of CO $_2$  to CO.

## 2. IR furnace cycle stability tests at ETHZ

A setup that allows multiple consecutive redox cycles is required to characterize materials and structures and benchmark those for their utilization in a solar fuel reactor. Ideally, the multiple cycles used for benchmarking would be performed faster than in the solar fuel reactor. In this manner, long-term cyclability tests can be carried out in short experimental campaigns. For this purpose, an experimental setup based on an infrared (IR) furnace has been built in the ETH Zürich laboratories. The IR furnace allows programmed cycling under varying temperatures and gas atmospheres (Figure 18). An infrared (IR) light source provides the energy to heat a sample inside the IR furnace quickly. The furnace is kept cold by an internal water-cooling circuit, which results in fast cooling when the power to the IR light sources is decreased. Hence, redox cycles can be performed employing heating and cooling rates exceeding  $300^{\circ}\text{C}\cdot\text{min}^{-1}$ . The studied sample, placed inside a sealed quartz tube, can be exposed to different atmosphere compositions by using three separate mass flow controllers (MFC) at the tube's inlet. A gas analyser measures the gas at the outlet to quantify  $\text{O}_2$  and  $\text{CO}$  produced to investigate the structure's chemical stability. A previous setup of the IR furnace setup has been used to demonstrate the stability of a small ceria reticulated porous ceramic (RPC) sample in 500 consecutive redox cycles [Marxer *et al.* 2017].

### 2.1. Experimental Procedures

A  $25\times 25\times 40$  mm ceria RPC sample is placed inside a quartz tube (ID  $\varnothing 38$  mm) and tested in a VHT-E48 infrared gold image furnace controlled by a Temperature Program Controller TPC 5000 (Advance Riko, inc.). A B-type thermocouple, shielded with an aluminium oxide jacket, measures the temperature inside the furnace (*Furnace Temperature*) and is used for the feedback control in the TPC. An S-type thermocouple is placed inside the sample to measure its temperature (*Sample Temperature*). The inlet gas flow (synthetic air, Ar,  $\text{CO}_2$ ) is controlled by three electronic mass flow controllers (MFC) (Bronkhorst Schweiz AG). The gasses flowing out of the furnace are directed to a gas analyser Ultramat 23 (Siemens AG), which measures oxygen, carbon dioxide, and carbon monoxide. A LabView program records the mass flows, gas

concentrations, and temperatures.

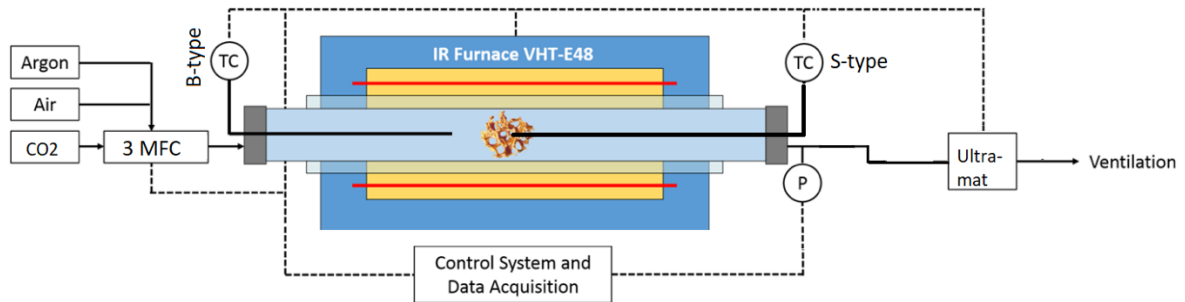


**Figure 18. IR furnace Experimental Setup. The sample is placed inside a sealed quartz tube. A B-type thermocouple (TC) measures the Furnace Temperature, and an S-type TC measures the Sample Temperature during the temperature and pressure cycling.**

The MFCs are calibrated using a MESALABS Definer 220, and the gas analyser (Ultramat 23) is calibrated using synthetic air and known gas mixture bottles.

### Temperature and Pressure Cycling

The cycling starts by heating the furnace to a predefined "low" or oxidation temperature while argon is fed. Once the system has been preheated, the Furnace temperature is ramped up to a "high" or reduction temperature. The temperature cycling is done between these two levels. During the ramp-up to reduction temperature, the ceria exceeds ca.1000°C, releasing oxygen. After roughly 5-15 minutes at reduction temperature, the feed gas is switched to CO<sub>2</sub>, and the temperature is ramped down to oxidation temperature. At this point, the ceria splits CO<sub>2</sub> into CO and O, incorporating the latter into its crystalline structure. A representative cycle is shown in Figure 19.

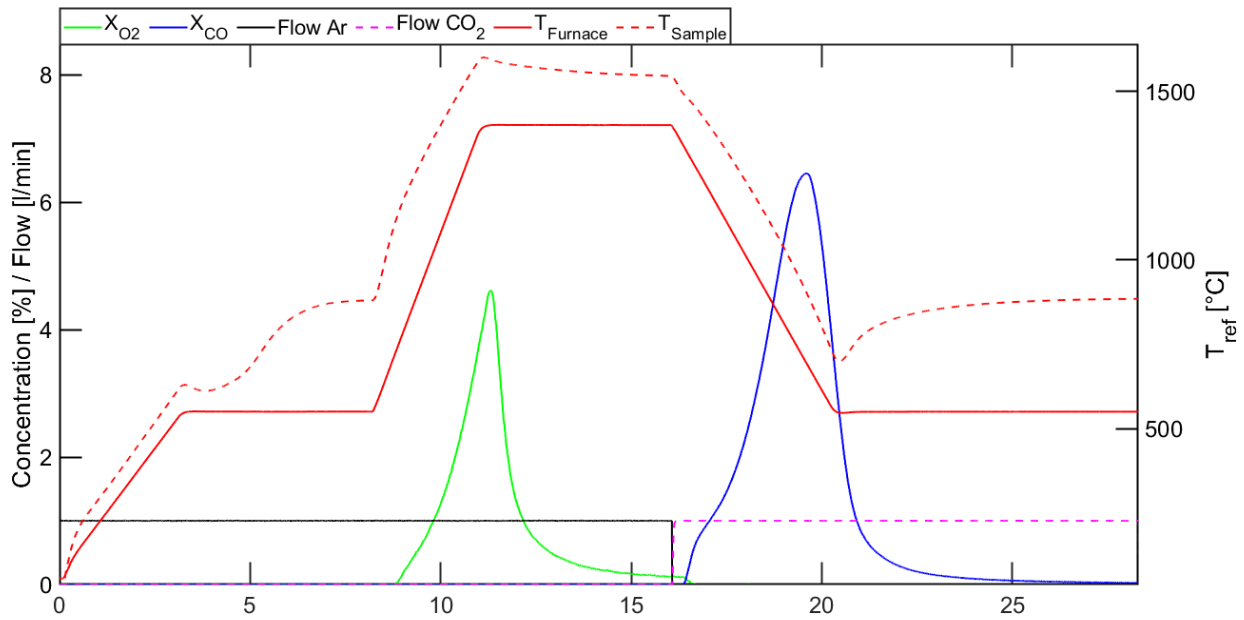


Figure 19. **One cycle in the IR Furnace. The Furnace Temperature and Sample Temperature are shown in solid-red and dashed-red lines, respectively (right y-axis). The O<sub>2</sub> concentration in green, CO concentration in blue, and the gas flows in black (Ar) and dashed-pink lines (CO<sub>2</sub>).**

The conditions used for the ceria RPC cycling are listed in Table 5.

<b>Table 5: Operating conditions for the ceria RPC cycling</b>		
<b>Step</b>	<b>Ramp / Dwell Time</b>	<b>Set Temperature</b>
Heat up from ambient	150°C/min	550°C
Heat up to reduction	280°C/min	1400°C
Reduction dwell time	5 mins	1400°C
Ramp down	212.5°C/min	550°C
Oxidation dwell time	8 mins	550°C
Cool down to ambient	150°C/min	250°C

Interestingly, the ceria changes its colour during reduction, increasing its absorption

coefficient [Ackermann and Steinfeld 2017]. For this reason, the *Sample Temperature* is several hundred degrees higher than the *Furnace Temperature* after the first cycle.

## Reaction Gases Volume Calculation

The released gas volumes can be calculated with the inlet gas flow and measured outlet concentrations. If the sample is reduced and oxidized to the same non-stoichiometry, CO to O<sub>2</sub> volumes should be in a 2:1 ratio, closing the mass balance.

The volume calculation is done in the following manner:

Reduction:

$$X_{O_2} = \frac{O_{2,outflow}}{O_{2,outflow} + Ar_{outflow}} = \frac{O_{2,outflow}}{O_{2,outflow} + Ar_{inflow}}$$

$$\dot{V}_{O_2} = O_{2,outflow} = \frac{X_{O_2}}{1 - X_{O_2}} Ar_{inflow}$$

$$V_{O_2} = \int \dot{V}_{O_2} dt = \int \frac{X_{O_2}}{1 - X_{O_2}} Ar_{inflow} dt$$

Oxidation:

$$X_{CO} = \frac{CO_{outflow}}{CO_{2,outflow} + CO_{outflow}} = \frac{CO_{outflow}}{CO_{2,inflow}}$$

$$\dot{V}_{CO} = CO_{outflow} = X_{CO} \cdot CO_{2,inflow}$$

$$V_{CO} = \int \dot{V}_{CO} dt = \int X_{CO} \cdot CO_{2,inflow} dt$$

## 2.2. Results

The ceria RPC withstood up to 79 cycles in one piece when a large crack split the sample. The tests were continued until 100 cycles were reached. The released gas volumes were relatively constant after an initial decrease. Moreover, the CO to O<sub>2</sub> ratio showed that the RPC was oxidizing back to its previous state in each cycle, and no side reactions occurred.

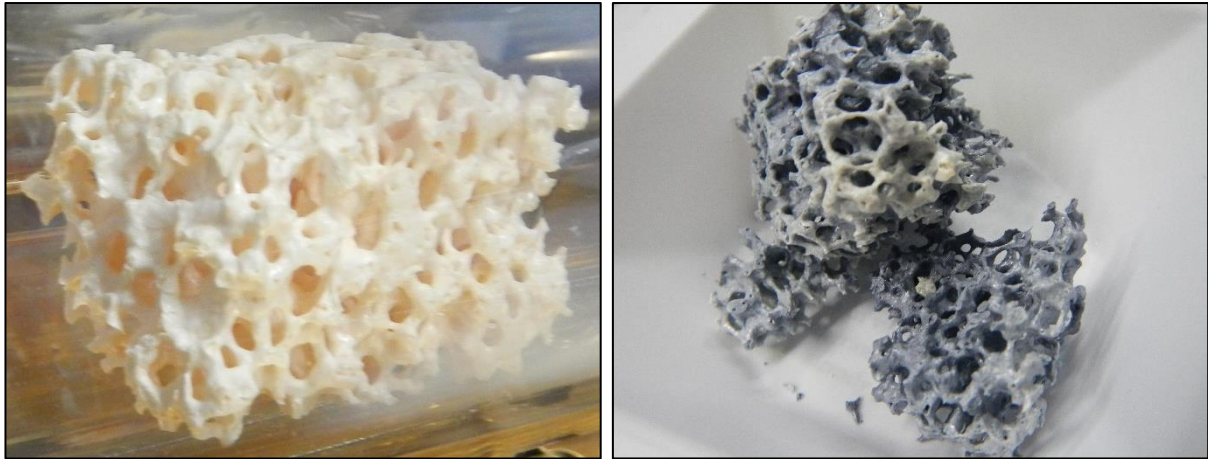


Figure 20. **RPC before the cycling (left) and the after 100 cycles (right)**

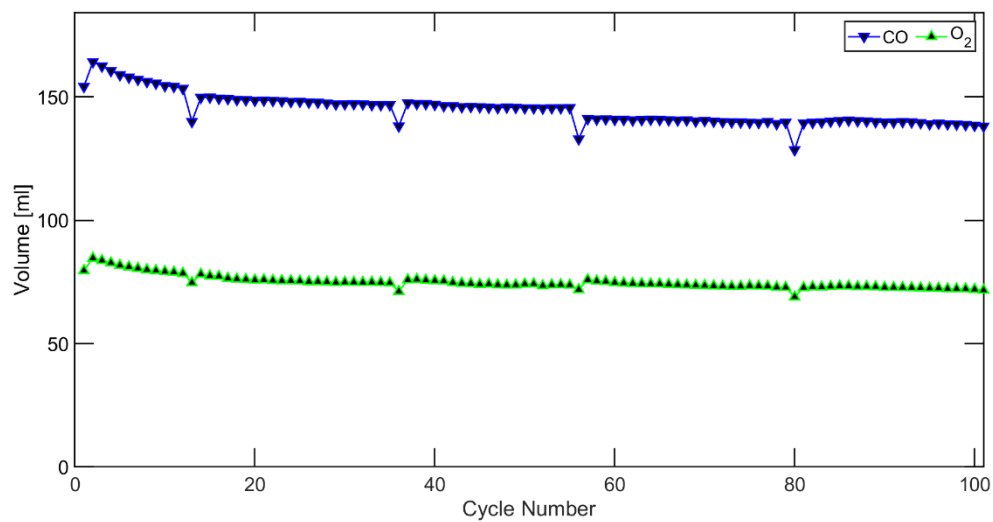


Figure 21. **Released CO and O<sub>2</sub> volumes over the cycles**

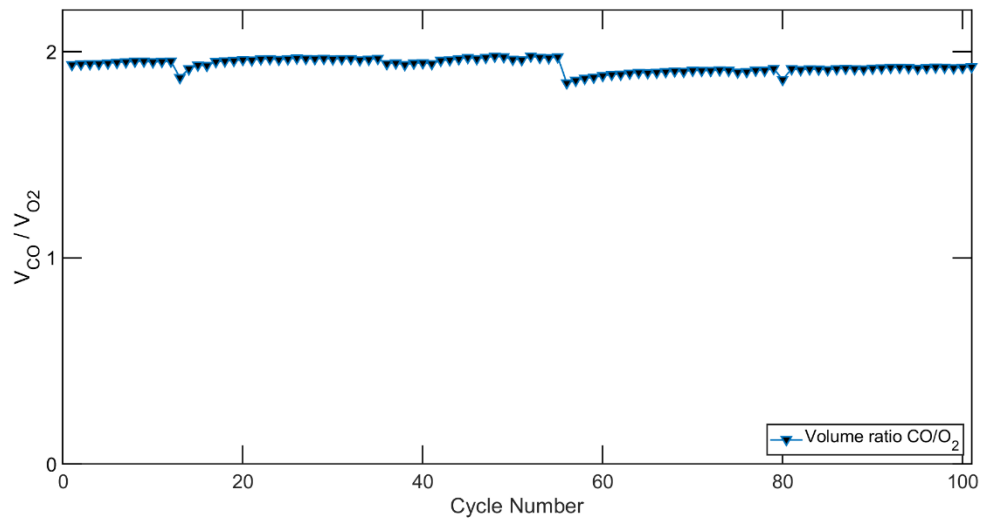


Figure 22. **Ratio of the released gas volumes for all cycles of the RPC**

## 2.3. Summary of procedures

A procedure to test the cyclability of materials and structures for the two-step thermochemical cycle has been built and implemented in the ETHZ Laboratories. The setup can be used to subject a sample to multiple cycles in a relatively short period, identifying mechanical and chemical degradation in the tested sample.

### 3. References

- Ackermann, S., & Steinfeld, A. (2017). Spectral hemispherical reflectivity of nonstoichiometric cerium dioxide. *Solar Energy Materials and Solar Cells*, 159, 167-171.
- Alonso, E., & Romero, M. (2015). Review of experimental investigation on directly irradiated particles solar reactors. *Renewable and sustainable energy reviews*, 41, 53-67.
- Bork, A. H., Carrillo, A. J., Hood, Z. D., Yildiz, B., & Rupp, J. L. (2020). Oxygen Exchange in Dual-Phase La<sub>0.65</sub>Sr<sub>0.35</sub>MnO<sub>3</sub>-CeO<sub>2</sub> Composites for Solar Thermochemical Fuel Production. *ACS Applied Materials & Interfaces*, 12(29), 32622-32632.
- Carrillo, A. J., González-Aguilar, J., Romero, M., & Coronado, J. M. (2019). Solar energy on demand: A review on high temperature thermochemical heat storage systems and materials. *Chemical reviews*, 119(7), 4777-4816.
- Oliveira, F. A. C., Barreiros, M. A., Abanades, S., Caetano, A. P., Novais, R. M., & Pullar, R. C. (2018). Solar thermochemical CO<sub>2</sub> splitting using cork-templated ceria ecoceramics. *Journal of CO<sub>2</sub> Utilization*, 26, 552-563.
- Giordano, F., Trovarelli, A., de Leitenburg, C., & Giona, M. (2000). A model for the temperature-programmed reduction of low and high surface area ceria. *Journal of catalysis*, 193(2), 273-282.
- Haeussler, A., Abanades, S., Julbe, A., Jouannaux, J., & Cartoixa, B. (2020). Solar thermochemical fuel production from H<sub>2</sub>O and CO<sub>2</sub> splitting via two-step redox cycling of reticulated porous ceria structures integrated in a monolithic cavity-type reactor. *Energy*, 201, 117649.
- Marxer, D., Furler, P., Takacs, M., & Steinfeld, A. (2017). Solar thermochemical splitting of CO<sub>2</sub> into separate streams of CO and O<sub>2</sub> with high selectivity, stability, conversion, and efficiency. *Energy & Environmental Science*, 10(5), 1142-1149.
- Matsukawa, T., Hoshikawa, A., Niwa, E., Yashima, M., & Ishigaki, T. (2018). Crystal structure of blue-colored ceria during redox reactions in a hydrogen atmosphere.

*CrystEngComm*, 20(2), 155-158.

Molinari, M., Parker, S. C., Sayle, D. C., & Islam, M. S. (2012). Water adsorption and its effect on the stability of low index stoichiometric and reduced surfaces of ceria. *The Journal of Physical Chemistry C*, 116(12), 7073-7082.

Muhich, C. L., Blaser, S., Hoes, M. C., & Steinfeld, A. (2018). Comparing the solar-to-fuel energy conversion efficiency of ceria and perovskite based thermochemical redox cycles for splitting H<sub>2</sub>O and CO<sub>2</sub>. *International Journal of Hydrogen Energy*, 43(41), 18814-18831.

Rhodes, N. R., Bobek, M. M., Allen, K. M., & Hahn, D. W. (2015). Investigation of long term reactive stability of ceria for use in solar thermochemical cycles. *Energy*, 89, 924-931.

Romero, M., & Steinfeld, A. (2012). Concentrating solar thermal power and thermochemical fuels. *Energy & Environmental Science*, 5(11), 9234-9245.

Wang, Y., & Makkee, M. (2018) The influence of CO<sub>2</sub> on NO reduction into N<sub>2</sub> over reduced ceria-based catalyst, *Applied Catalysis B: Environmental*, 221, 196–205.

Warren, K. J., Tran J. T., Weimer A. W. (2022), A thermochemical study of iron aluminate-based materials: a preferred class for isothermal water splitting, *Energy & Environmental Science*. Advanced article

Yao, H. C., & Yao, Y. Y. (1984). Ceria in automotive exhaust catalysts: I. Oxygen storage. *Journal of catalysis*, 86(2), 254-265..

Zoller, S., Koepf, E., Roos, P., & Steinfeld, A. (2019). Heat transfer model of a 50 kW solar receiver–reactor for thermochemical redox cycling using cerium dioxide. *Journal of Solar Energy Engineering*, 141(2).